NETWORKS AND HETEROGENEOUS MEDIA
©American Institute of Mathematical Sciences
Volume **6**, Number **3**, September **2011**

doi:10.3934/nhm.2011.6.401

pp. **401–423**

AN ADAPTIVE FINITE-VOLUME METHOD FOR A MODEL OF TWO-PHASE PEDESTRIAN FLOW

Stefan Berres

Departamento de Ciencias Matemáticas y Físicas
Universidad Católica de Temuco
Temuco, Chile

Ricardo Ruiz-Baier

Modeling and Scientific Computing, MATHICSE
Ecole Polytechnique Fédérale de Lausanne
CH-1015 Lausanne, Switzerland

Hartmut Schwandt

Institut für Mathematik, Fakultät II Mathematik und Naturwissenschaften
Technische Universität Berlin, Straße des 17. Juni 136
D-10623 Berlin, Germany

Elmer M. Tory

Department of Mathematics and Computer Science
Mount Allison University
Sackville, NB E4L 1G6, Canada

Abstract. A flow composed of two populations of pedestrians moving in different directions is modeled by a two-dimensional system of convection-diffusion equations. An efficient simulation of the two-dimensional model is obtained by a finite-volume scheme combined with a fully adaptive multiresolution strategy. Numerical tests show the flow behavior in various settings of initial and boundary conditions, where different species move in countercurrent or perpendicular directions. The equations are characterized as hyperbolic-elliptic degenerate, with an elliptic region in the phase space, which in one space dimension is known to produce oscillation waves. When the initial data are chosen inside the elliptic region, a spatial segregation of the populations leads to pattern formation. The entries of the diffusion-matrix determine the stability of the model and the shape of the patterns.

1. **Introduction.** In the description and modeling of pedestrian behavior it is common sense to apply a rough classification by distinguishing between microscopic and macroscopic models [18]. Macroscopic models focus on the balancing relationships of particle (i. e. pedestrian) density, flow intensity and flow speed etc. In microscopic models, pedestrians are considered as individual objects interacting with each other, while in macroscopic models, pedestrian behavior is analyzed in terms of more global properties of a continuous stream. For a detailed overview of both vehicular and pedestrian traffic and the main modeling and simulation approaches, we refer to [25].

2000 *Mathematics Subject Classification.* Primary: 92D25, 35L65; Secondary: 65M50.
Key words and phrases. Crowd model, Multiphase flow, System of conservation laws, Mixed hyperbolic-elliptic system, Elliptic region, Fully adaptive multiresolution.

The modeling of pedestrian flows using macroscopic approaches has received several contributions in the last decade [8, 10, 27, 30, 39, 45]. In particular, it has been observed that in dense pedestrian crowds, pedestrians behave quite similarly to gas particles. This was one important reason to model pedestrian flows by fluid physical models from gas or fluid dynamics. Most of the research in the macroscopic area of pedestrian simulation is, therefore, focussed on the discussion and development of general partial differential equations, one- and two-dimensional in space, based on physical principles like mass, momentum and energy balance. Social and physical force models resulting from microscopic modeling are included as outer force terms in only a few papers. In [24], e.g., two-dimensional density and pressure fields were illustrated, which were mostly obtained by collecting results of microscopic social force models.

With some heuristic assumptions, different models have been derived based on the Boltzmann equation and conservation laws ([31], [35], e.g.). These models can be considered as special cases of the continuity or density equation and the momentum/velocity equation. To derive the classical Euler equation (without viscous terms) it is necessary to assume that the velocity distribution is approximately equal to the equilibrium/Gaussian distribution. Approaches based on the Navier-Stokes equation can be derived without the equilibrium assumption. The equations differ from classical fluid or gas dynamic equations mostly by the source term in the momentum equation to describe social and physical forces acting on and by pedestrians. A comprehensive overview of macroscopic models of pedestrian flows is given in [25].

On the other hand, there exists a large number of microscopic approaches based on ordinary differential equations, cellular automata or graph theory. We refer again to [25]. Among these models, cellular automata are very prominent since they use intuitive physical assumptions and are quickly implemented. They have been adapted to both vehicular traffic ([19], e.g.) and pedestrian dynamics ([13], e.g.). An approach described in [15] will be used in future work of the present context. The advantage of cellular automata and similar discrete models is that they are very flexible in engineering ad-hoc assumptions. In addition, they allow agent (person or car) tracking rather than only counting densities.

A new hybrid approach [16, 40] describes a combined microscopic and macroscopic modeling in a multiscale framework using a measure-theoretic approach. The crowd velocity is composed as a sum of a macro-scale desired velocity and a micro-scale interaction velocity that accounts for an explicit local control in a small neighborhood. A control mechanism considers a local movement that is based on the situation in a small neighborhood and is directed away from a center of mass or, similarly, towards a so-called inverse center of mass.

The idea of considering traffic flow in the context of continuum mechanics was first formulated in the Lighthill-Whitham-Richards (LWR) model [35, 41], where traffic dynamics are described by the scalar one-dimensional conservation law

$$u_t + f(u)_x = 0. \tag{1}$$

The unknown variable $u = u(x,t)$ denotes a locally averaged car-density assigned at each time t and each position x. The flux function

$$f(u) = auV(u)$$

encapsulates the model assumptions concerning the average velocity of cars. Here, a is a constant that corresponds to the maximum velocity and $V = V(u)$ is a

normalized density-dependent velocity function. As a simple and early example of this function we mention Greenshield's model

$$V(u) = 1 - (u/u_{\max})^n \tag{2}$$

with $n > 0$ and $u_{\max} \in (0, 1)$. Among the first generalizations of the scalar LWR model is the two-phase traffic-flow model proposed by Bick and Newell [9]

$$u_t + (u(1 - u - \beta v))_x = 0, \qquad v_t + (-v(1 - \beta u - v))_x = 0, \tag{3}$$

with $\beta > 0$, which describes the flow in opposite directions that are mutually affected. In more general multiphase traffic-flow models, the unknown variables represent several phases corresponding to different lanes or car types [4].

Simulation models for *vehicular traffic* have a more or less one-dimensional character as cars move in lanes on streets allowing cross-directional flow only at distinct crossing points. In contrast, pedestrian flow allows a genuine spatial structure: pedestrian movement can be directed principally to any direction and it is strongly influenced by human behavior. Therefore, simulation models for pedestrian traffic are two- (or even three-)dimensional.

A well known problem which has been thoroughly studied in particular by microscopical models is the *escape* or *evacuation problem*, where the task is to model escape panic([23], e.g.). In an escape situation, all individuals de facto try to reach the same destination. Therefore, escape problems can be formally considered as single destination problems which can be modeled by a unique pedestrian stream. The modeling of multi-destination problems characterized by at least two distinct pedestrian streams remains a specifically difficult and not yet deeply investigated challenge, in particular if one assumes that each stream has its own, unique target direction. Both microscopic and macroscopic approaches are suitable.

In this paper, we will follow a macroscopic approach. A generalization of (1) to two-dimensional multiple-species pedestrian flow is proposed in [28]. It is based on mass equations having the form

$$\boldsymbol{u}_t + \boldsymbol{f}(\boldsymbol{u})_x + \boldsymbol{g}(\boldsymbol{u})_y = 0,$$

where $\boldsymbol{f}$ and $\boldsymbol{g}$ are the fluxes in x and y directions, respectively. The emphasis in [28] was on a first modeling and justification of pedestrians' motion by continuum theory. It treated a specific situation with a preliminary use of numerical methods that were adapted to a specific example, but did not elaborate the dynamics of the phase-separation phenomenon.

In the present paper, we develop a multiphase model using two-dimensional convection-diffusion systems by modifying the above equation. The intention is to show that this approach is well suited for the description and simulation of various aspects of pedestrian traffic, especially in the case of crossings of multiple streams. We attack a twofold task. On the one hand, we intend to relate some mathematical properties resulting from continuum theory to phenomenological properties of pedestrian movement in specific situations. On the other hand, we start to develop a robust simulation model. Concerning the latter task, this paper has to be considered as a first step to a more general simulation model which is under development. We start with a purely macroscopic approach and investigate up to which extent aspects of pedestrian flow can be adequately modeled in the above context. The limitations of purely macroscopic models we can expect are due to the fact that pedestrians are not 'infinitely small' gas molecules and are not compressible. They require a minimal physical space, the range of possible values for the walking speed

is restricted and, most important, their movements are also strongly influenced by individual behavior and individual decisions. As a consequence, macroscopic models have to be complemented by additional elements. This will be the subject of the further development. This aspect is principally known. As examples for such approaches we mention [16, 40] or [42, 43].

One of the aims of this paper is to put pedestrian flow in the context of existing lines of continuum theory with similar phenomenological properties. The focus is on numerical issues in that context, studies of the separation behavior in idealized test situations and, in particular, on the elliptic-hyperbolic type behavior of the underlying equations. In some specific situations, crowds, where two groups of pedestrians move in opposite directions, can have a phenomenological behavior similar to bidisperse suspensions in which one solid species is heavier than the fluid and the other lighter. In experiments with bidisperse suspensions at low concentrations (corresponding to the hyperbolic region in the continuum approach), the two species move by each other with little interference, which is also typical of light pedestrian-flow in opposite directions. At higher concentrations, the suspension separates into upward- and downward-moving streams [11]. This corresponds to the change in the system of equations from hyperbolic to elliptic. The striking agreement between the theoretical and experimental results for bidisperse suspensions [11] offers hope that a similar result may occur for opposing streams of pedestrians in appropriate situations.

For the numerical simulation, we use a finite-volume scheme ([44], e.g.). For the simulation of traffic flow modeled by spatially one-dimensional systems of conservation laws, high-resolution methods deliver satisfactorily accurate results [46]. In the numerical experiments we use the *local* Lax-Friedrichs flux, which falls into the class of central numerical fluxes and keeps the robustness and simplicity of the Lax-Friedrichs flux, but gains a sharper resolution by the use of a local estimation of the maximum wave-speeds [34]. The sharp interfaces that occur during phase separation in multiphase crowd models are resolved with help of a fully adaptive multiresolution scheme.

We have organized the remainder of this paper as follows. In Section 2 we give two short resumés on the mathematical background of the subsequent discussion related to continuum theoretical aspects and the context of the intended simulation model. Section 3 outlines the model for the interaction between two species of pedestrians. Section 4 provides a description of the finite-volume method and the multiresolution analysis employed in the numerical approximation. Section 5 contains several numerical examples that exhibit some of the predicted features of the model, and finally we draw some conclusions and possible extensions in Section 6.

2. **Modeling and simulation context.**

In order to improve the motivation of the considered simulation model we briefly outline (a) the context of mixed hyperbolic-elliptic systems and (b) the context in which the intended simulation model will be developed.

2.1. **Mixed systems and elliptic regions.**

A special property of the Bick-Newell model (3) is that its phase space contains an elliptic region. An elliptic state in the solution space is a state where the Jacobian matrix of the vector-valued flux function has complex eigenvalues. The set of all elliptic points forms the elliptic region. This contribution promotes a physical interpretation of the formal property of elliptic regions. It is argued that, in a two-dimensional setting, the elliptic degeneracy of

the system can trigger spatial phase separation. Therefore, crowd models can be considered to give a prototype physical explanation of mixed systems. To put this in an appropriate context, a short resumé on mixed hyperbolic-elliptic systems is given in this subsection.

Hyperbolic-elliptic systems were first studied for porous-media flow in [3], where a series of Riemann problems are solved numerically by a finite-difference scheme. The choice of initial data in the form of two distinct states inside the elliptic region leads to a transition from one state to the other via two loops around the elliptic region. See [2, 37] for more recent descriptions of multiphase flow described by mixed hyperbolic-elliptic systems occurring in porous media. Solutions of Riemann problems with a quadratic flux function corresponding to an idealized porous-media flow model have been classified in [26]. The effect of changing the diffusion matrix on the solution of Riemann problems has been studied in [14, 29]. In [36] the effect of a regularization with a viscosity matrix on an instability related to the elliptic region is examined. For a general overview of mixed hyperbolic-elliptic systems, their appearance and applications, see [20, 32, 33].

In [21], the solution is confined to the elliptic region in order to study the phenomenon of 'oscillation waves' in more detail. When the constant initial data inside the elliptic region are perturbed in a few points, the finite-difference scheme produces oscillation waves. These oscillation waves satisfy the Rankine-Hugoniot condition in an average sense and thus can be formally interpreted as measure-valued solutions. There is a tendency for the solution to avoid the elliptic region, i.e., initial data inside move rapidly towards the boundaries and even exit the region. In two space dimensions, this avoidance tendency might lead to fingering effects and pattern formation.

In dispersed particle flow, there is experimental evidence of phase-separation behavior (such as forming channels) that can be related to the elliptic region. A characterization of a series of models for polydisperse suspensions with respect to the appearance of elliptic regions has been carried out [11]. This study is continued in [6], where, for a specific model, oscillation waves are simulated and it is shown how the shape of the elliptic region can be controlled by the choice of model parameters. A combination of classical and oscillation waves can be generated when one Riemann state is chosen inside the elliptic region and the other outside. However, when the Riemann data are chosen outside the elliptic region, they do not enter but seem to avoid it. Rather, when perturbed constant data are chosen inside the elliptic region, which is not tangent to all axes of the phase space of permitted solution values, the solution escapes the elliptic region and a non-oscillatory stationary state is formed.

2.2. **Towards a simulation model for pedestrian flow.** In Euler/Navier-Stokes based models, we are faced with the undesirable side effect that momentum conservation has to be considered, which contradicts somewhat pedestrian behavior which is influenced by individual decisions at least as long as there is physical space for movement. The subsequently developed, more simple convection-diffusion approach allows us to circumvent this problem.

The multiphase approach will enable us to model each of two or more pedestrian streams as a separate phase. One of the fundamental problems in using continuous macroscopic approaches derived from flow models is that gases or liquids merge by diffusion or build vortices and similar structures which are accompanied by direction changes that are not necessarily typical for pedestrian movement. In the present context, we consider in particular the problem of two or more pedestrian streams,

each having a specific destination, which intersect and continue to their destination after crossing. In addition, we assume that all pedestrians remain in their stream, i.e. that phase change after crossing does not occur.

Obviously, purely macroscopic approaches derived from flow models become more realistic for high densities. With decreasing densities, the 'discrete' aspects of pedestrian movement become more significant. As a consequence, it is favorable to complete simulation models for pedestrian movement in (not only) our context by elements describing both local individual interaction and tactical instruments to keep or resume the way to the intended final destination. As a first step, however, we study the benefits and limitations of a purely macroscopic approach (without the above additions) in the present paper by presenting the model framework and a series of numerical examples.

3. Two-species pedestrian model.

The two-dimensional pedestrian-flow model describing the spatial interaction of two species of pedestrians is formulated as the system of two convection-diffusion equations

$$\begin{aligned} u_t + \partial_x f_1(u,v;x,y) + \partial_y g_1(u,v;x,y) &= \nabla\cdot\big(b_{11}(u,v)\nabla u)\big) + \nabla\cdot\big(b_{12}(u,v)\nabla v)\big),\\ v_t + \partial_x f_2(u,v;x,y) + \partial_y g_2(u,v;x,y) &= \nabla\cdot\big(b_{21}(u,v)\nabla u)\big) + \nabla\cdot\big(b_{22}(u,v)\nabla v)\big), \end{aligned} \tag{4}$$

in $\Omega_T = \Omega\times(0,T)$, where u, v denote the densities of the two distinct pedestrian species in the spatial domain $\Omega\subset\mathbb{R}^2$. The model can be extended to more than two phases.

In the parabolic part, the functions $b_{11}(u,v)$, $b_{22}(u,v)$ account for self-diffusion, whereas the functions $b_{12}(u,v)$, $b_{21}(u,v)$ represent a cross-diffusion that can be interpreted as an avoidance strategy of the respective other species. Such a tendency away from regions occupied by the other species is known for epidemic models, where a susceptible population avoids the infected population [1, 7]. When the diffusion terms are small, the equations are dominated by convection, and thus they need a careful discretization. The presence of the position (x,y) in the fluxes f, g allows the species movement to depend on location. This permits us to design a location-dependent direction which applies, e.g., when targeting an exit. With the notation

$$\begin{aligned} \boldsymbol{u} &= \begin{pmatrix} u\\ v\end{pmatrix}, \quad \boldsymbol{f}(\boldsymbol{u};\boldsymbol{x}) = \begin{pmatrix} f_1(u,v;x,y)\\ f_2(u,v;x,y)\end{pmatrix},\\ \boldsymbol{g}(\boldsymbol{u};\boldsymbol{x}) &= \begin{pmatrix} g_1(u,v;x,y)\\ g_2(u,v;x,y)\end{pmatrix}, \ \boldsymbol{b}(\boldsymbol{u}) = \begin{pmatrix} b_{11}(u,v) & b_{12}(u,v)\\ b_{21}(u,v) & b_{22}(u,v)\end{pmatrix}, \end{aligned}$$

the system (4) is written in compact form as

$$\frac{d}{dt}\boldsymbol{u} + \partial_x\boldsymbol{f}(\boldsymbol{u};\boldsymbol{x}) + \partial_y\boldsymbol{g}(\boldsymbol{u};\boldsymbol{x}) = \nabla\cdot\Big(\boldsymbol{b}(\boldsymbol{u})\nabla\boldsymbol{u}\Big). \tag{5}$$

In generalizing the LWR model to two space dimensions, the main issue is to determine the directions of the flow. Pedestrian flow in two space dimensions follows the same physical principles as in its reduction to one space dimension. The main difference is that the *total flux* of a species, which describes the overall movement, is distributed to the directions. Before splitting the flux components into directions, we must define the total flux, which is the flux in the direction of principal movement. Let $h_1(u,v)$, $h_2(u,v)$ denote the total fluxes for species 1 and 2, respectively.

These total fluxes are then distributed in the x and y directions. If the fluxes are singly directed, the two-dimensional system (4) reduces to the one-dimensional one

$$u_t + \partial_x h_1(u,v) = \partial_x\big(b_{11}(u,v)\partial_x u\big) + \partial_x\big(b_{12}(u,v)\partial_x v\big),$$
$$v_t + \partial_x h_2(u,v) = \partial_x\big(b_{21}(u,v)\partial_x u\big) + \partial_x\big(b_{22}(u,v)\partial_x v\big).$$

The total fluxes are specified for each species as in the one-dimensional setting by

$$h_1(u,v) = a_1 u V(u,v), \quad h_2(u,v) = a_2 v V(u,v),$$

with $a_i > 0,\ i = 1,2$. More compactly, we have

$$\mathbf{h}(\boldsymbol{u}) = \begin{pmatrix} h_1(u,v) \\ h_2(u,v) \end{pmatrix} = \begin{pmatrix} a_1 u \\ a_2 v \end{pmatrix} V(u,v). \tag{6}$$

The velocity function $V(u,v)$ follows the suggestions for scalar equations, e.g.

$$V(\boldsymbol{u}) = 1 - \|\boldsymbol{u}\|_1, \quad \text{i.e,} \quad V(u,v) = 1 - u - v,$$

which is an extension of Greenshield's model (2) with $n = 1$ and $u_{\max} = 1$. Obviously, other choices are admissible. A parameter choice $a_1 = 1,\ a_2 = -1$ reduces in one space dimension to the Bick-Newell model (3) with $\beta = 1$. In the multi-dimensional setting, the different flow directions are not expressed by the sign, but by a direction matrix.

The fluxes $\boldsymbol{f}, \boldsymbol{g}$ in (5) are composed by a total flux $\mathbf{h}$ and a direction contribution, which distributes the total local flow of a species as

$$\begin{aligned} f_1(u,v;x,y) &= h_1(u,v) d_1^{\mathrm{x}}(x,y), \quad & g_1(u,v;x,y) &= h_1(u,v) d_1^{\mathrm{y}}(x,y), \\ f_2(u,v;x,y) &= h_2(u,v) d_2^{\mathrm{x}}(x,y), \quad & g_2(u,v;x,y) &= h_2(u,v) d_2^{\mathrm{y}}(x,y). \end{aligned} \tag{7}$$

The directions can be formally put into a direction matrix

$$D = \begin{pmatrix} d_1^{\mathrm{x}}(x,y) & d_1^{\mathrm{y}}(x,y) \\ d_2^{\mathrm{x}}(x,y) & d_2^{\mathrm{y}}(x,y) \end{pmatrix} = \left(\begin{array}{c} \boldsymbol{d}_1(\boldsymbol{x}) \\ \hline \boldsymbol{d}_2(\boldsymbol{x}) \end{array}\right) = \left(\boldsymbol{d}^{\mathrm{x}}(\boldsymbol{x}) \quad | \quad \boldsymbol{d}^{\mathrm{y}}(\boldsymbol{x})\right),$$

where the subscripts (1 or 2) denote the species and the superscripts (x or y) denote the direction component. The direction matrix combines components for both species and directions. E.g., $d_1^y(x,y)$ denotes that fraction of the flux of species 1 that flows in the y direction. The direction matrix can be decomposed either by species with the row vectors $\boldsymbol{d}_1(\boldsymbol{x}),\ \boldsymbol{d}_2(\boldsymbol{x})$ or by directions with the column vectors $\boldsymbol{d}^{\mathrm{x}}(\boldsymbol{x}),\ \boldsymbol{d}^{\mathrm{y}}(\boldsymbol{x})$.

Allocating (7) by the vector-valued fluxes $\boldsymbol{f}, \boldsymbol{g}$, using the specification of the total fluxes (6) gives

$$\boldsymbol{f}(u,v;x,y) = \begin{pmatrix} a_1 u V(u,v) d_1^{\mathrm{x}}(x,y) \\ a_2 v V(u,v) d_2^{\mathrm{x}}(x,y) \end{pmatrix}, \quad \boldsymbol{g}(u,v;x,y) = \begin{pmatrix} a_1 u V(u,v) d_1^{\mathrm{y}}(x,y) \\ a_2 v V(u,v) d_2^{\mathrm{y}}(x,y) \end{pmatrix}.$$

The discretization via numerical fluxes is based on this definition of the vector-valued fluxes. Denoting component-wise multiplication by $\otimes$, we can write compactly

$$\boldsymbol{f}(\boldsymbol{u};\boldsymbol{x}) = \boldsymbol{h}(\boldsymbol{u}) \otimes \boldsymbol{d}^{\mathrm{x}}(\boldsymbol{x}), \quad \boldsymbol{g}(\boldsymbol{u};\boldsymbol{x}) = \boldsymbol{h}(\boldsymbol{u}) \otimes \boldsymbol{d}^{\mathrm{y}}(\boldsymbol{x}). \tag{8}$$

The direction for each species has to be normalized in order to satisfy

$$\|(f_1, g_1)(u,v;x,y)\|_2 = |h_1(u,v)|, \quad \|(f_2, g_2)(u,v;x,y)\|_2 = |h_2(u,v)|,$$

for all u, v, x, y i.e., the magnitude of the flux for one species (even if distributed in various directions) is determined by its total flux. This normalization is accomplished by prescribing that the direction vectors

$$\mathbf{d}_1(\boldsymbol{x}) = \begin{pmatrix} d_1^{\mathrm{x}}(x,y) & d_1^{\mathrm{y}}(x,y) \end{pmatrix}, \qquad \mathbf{d}_2(\boldsymbol{x}) = \begin{pmatrix} d_2^{\mathrm{x}}(x,y) & d_2^{\mathrm{y}}(x,y) \end{pmatrix},$$

satisfy

$$\|\boldsymbol{d}_1(\boldsymbol{x})\|_2 = 1, \quad \|\boldsymbol{d}_2(\boldsymbol{x})\|_2 = 1 \quad \text{for all} \quad \boldsymbol{x} \in \Omega. \tag{9}$$

The model of Hughes [28] specifies the directions employing the potentials ϕ, ψ associated with phases 1 and 2, respectively, as

$$d_1^{\mathrm{x}}(x,y) = \frac{\phi_x}{\|\nabla\phi\|_2}, \quad d_1^{\mathrm{y}}(x,y) = \frac{\phi_y}{\|\nabla\phi\|_2}, \quad d_2^{\mathrm{x}}(x,y) = \frac{\psi_x}{\|\nabla\psi\|_2}, \quad d_2^{\mathrm{y}}(x,y) = \frac{\psi_y}{\|\nabla\psi\|_2},$$

where the gradient norms

$$\|\nabla\phi\|_2 = \sqrt{\phi_x^2 + \phi_y^2}, \qquad \|\nabla\psi\|_2 = \sqrt{\psi_x^2 + \psi_y^2}$$

ensure that (9) holds. In a generalization of the model, the directions could also depend on the pedestrian concentrations u and v.

4. Finite volume formulation.

This section deals with the formulation of a fully adaptive multiresolution scheme for numerically solving the convection diffusion system (4). Given the convection-dominated nature of the underlying problem, space-adaptive methods represent an adequate tool for accurately capturing the wave fronts at a reduced computational cost.

Let $\mathcal{T}^0 \subset \cdots \mathcal{T}^\ell \cdots \subset \mathcal{T}^H$ be a family of nested admissible rectangular meshes, that is, partitions of Ω formed by control volumes K^ℓ (open rectangles of maximum diameter h_{K^ℓ}) and constrained by the condition that the segment joining the centers of two neighboring control volumes x_{K^ℓ} and x_{L^ℓ} must be orthogonal to the corresponding interface $\sigma = \sigma(K^\ell, L^\ell)$. By $\mathcal{E}(K^\ell)$, $\mathcal{E}_{\mathrm{int}}(K^\ell)$ we denote the set of edges of K^ℓ, and its restriction to boundary edges. We denote by $\mathcal{E}_{\mathrm{int}}^\ell$ and $\mathcal{E}_{\mathrm{ext}}^\ell$ the sets of all edges in the interior of $\mathcal{T}^\ell$ and lying on the boundary $\partial\Omega$, respectively. For each cell L^ℓ neighbor to K^ℓ, $d(K^\ell, L^\ell)$ denotes the distance between x_{K^ℓ} and x_{L^ℓ}.

4.1. A finite-volume formulation.

In order to define the discrete marching formula for (4), we choose an admissible discretization of Ω_T consisting of an admissible mesh $\mathcal{T}^\ell$ of Ω and a time-step size $\Delta t > 0$. We may choose $N > 0$ as the smallest integer such that $N\Delta t \geq T$, and set $t^n := n\Delta t$ for $n \in \{0, \ldots, N\}$.

We denote the cell averages of u and v on $K^\ell \in \mathcal{T}^\ell$ at time $t = t^n$ by

$$u_{K^\ell}^n := \frac{1}{|K^\ell|}\int_{K^\ell} u(x, t^n)\, dx, \quad v_{K^\ell}^n := \frac{1}{|K^\ell|}\int_{K^\ell} v(x, t^n)\, dx.$$

The resulting finite-volume scheme for the approximation of (4), defined on the resolution level ℓ, assumes values $u_{K^\ell}^n$ and $v_{K^\ell}^n$ for all $K^\ell \in \mathcal{T}^\ell$ at time $t = t^n$ and determines $u_{K^\ell}^{n+1}$ and $v_{K^\ell}^{n+1}$ for all $K^\ell \in \mathcal{T}^\ell$ at time $t = t^{n+1} = t^n + \Delta t$ by a marching formula. With the compact notation

$$\boldsymbol{F} = (\boldsymbol{f}, \boldsymbol{g}) = \begin{pmatrix} f_1 & g_1 \\ f_2 & g_2 \end{pmatrix},$$

and using a standard finite-volume approach, the system (4) is discretized as

$$|K^\ell|\frac{\boldsymbol{u}_{K^\ell}^{n+1}-\boldsymbol{u}_{K^\ell}^{n}}{\Delta t}-\sum_{\sigma\in\mathcal{E}_{\mathrm{int}}(K^\ell)}\frac{|\sigma(K^\ell,L^\ell)|}{d(K^\ell,L^\ell)}\Bigg(\boldsymbol{F}\big(\boldsymbol{u}_{K^\ell}^{n},\boldsymbol{u}_{L^\ell}^{n};\bar{\boldsymbol{x}}(K^\ell,L^\ell);\boldsymbol{n}(K^\ell,L^\ell)\big)\cdot \boldsymbol{n}(K^\ell,L^\ell)+\frac{\boldsymbol{b}(\boldsymbol{u}_{L^\ell}^{n})+\boldsymbol{b}(\boldsymbol{u}_{K^\ell}^{n})}{2}\big(\boldsymbol{u}_{L^\ell}^{n}-\boldsymbol{u}_{K^\ell}^{n}\big)\Bigg), \tag{10}$$

where $\boldsymbol{n}(K^\ell,L^\ell)=\big(n_1(K^\ell,L^\ell),n_2(K^\ell,L^\ell)\big)^{\mathrm{T}}$ is the outer normal vector of cell K^ℓ pointing towards L^ℓ such that

$$\begin{aligned}\boldsymbol{F}\big(\boldsymbol{u}_{K^\ell}^{n},\boldsymbol{u}_{L^\ell};\bar{\boldsymbol{x}}(K^\ell,L^\ell);\boldsymbol{n}(K^\ell,L^\ell)\big)\cdot\boldsymbol{n}(K^\ell,L^\ell)&\\ =\boldsymbol{f}\big(\boldsymbol{u}_{K^\ell}^{n},\boldsymbol{u}_{L^\ell}^{n};\bar{\boldsymbol{x}}(K^\ell,L^\ell);\boldsymbol{n}(K^\ell,L^\ell)\big)\cdot n_1(K^\ell,L^\ell)&\\ +\boldsymbol{g}\big(\boldsymbol{u}_{K^\ell}^{n},\boldsymbol{u}_{L^\ell}^{n};\bar{\boldsymbol{x}}(K^\ell,L^\ell);\boldsymbol{n}(K^\ell,L^\ell)\big)\cdot n_2(K^\ell,L^\ell).&\end{aligned}$$

Here, the numerical fluxes

$$\boldsymbol{f}\big(\boldsymbol{u}_{K^\ell}^{n},\boldsymbol{u}_{L^\ell};\bar{\boldsymbol{x}}(K^\ell,L^\ell);\boldsymbol{n}(K^\ell,L^\ell)\big),\quad \boldsymbol{g}\big(\boldsymbol{u}_{K^\ell}^{n},\boldsymbol{u}_{L^\ell};\bar{\boldsymbol{x}}(K^\ell,L^\ell);\boldsymbol{n}(K^\ell,L^\ell)\big)$$

depend on both of the components $\boldsymbol{u}_{K^\ell}^{n}$ and $\boldsymbol{u}_{L^\ell}^{n}$ on the sides of the cell interface; $\bar{\boldsymbol{x}}(K^\ell,L^\ell)$ is the position of the midpoint of the interface between cell K^ℓ and L^ℓ. Moreover, $(\boldsymbol{b}(\boldsymbol{u}_{L^\ell}^{n})+\boldsymbol{b}(\boldsymbol{u}_{K^\ell}^{n})/2$ corresponds to a component-wise average of the diffusion matrix $\boldsymbol{b}$. This averaged matrix is multiplied by the vector difference $\boldsymbol{u}_{L^\ell}^{n}-\boldsymbol{u}_{K^\ell}^{n}$ such that the summation over all volumes resembles a central difference for the parabolic term. In [7], this non-conservative discretization of the parabolic term is compared to a conservative discretization. The multiresolution setting produces such an accurate resolution that no differences can be detected for a non-linear diffusion matrix. For a constant diffusion matrix both discretizations are equivalent.

Making use of the rectangular grid structure, we calculate the two-dimensional numerical fluxes as

$$\boldsymbol{F}\big(\boldsymbol{u}_{K^\ell}^{n},\boldsymbol{u}_{L^\ell}^{n};\boldsymbol{n}(K^\ell,L^\ell)\big)\cdot\boldsymbol{n}(K^\ell,L^\ell)\big)=\begin{cases}\boldsymbol{f}(\boldsymbol{u}_{K^\ell}^{n},\boldsymbol{u}_{L^\ell}^{n}) & \text{if}\quad \boldsymbol{n}=(1,0),\\ \boldsymbol{f}(\boldsymbol{u}_{L^\ell}^{n},\boldsymbol{u}_{K^\ell}^{n}) & \text{if}\quad \boldsymbol{n}=(-1,0),\\ \boldsymbol{g}(\boldsymbol{u}_{K^\ell}^{n},\boldsymbol{u}_{L^\ell}^{n}) & \text{if}\quad \boldsymbol{n}=(0,1),\\ \boldsymbol{g}(\boldsymbol{u}_{L^\ell}^{n},\boldsymbol{u}_{K^\ell}^{n}) & \text{if}\quad \boldsymbol{n}=(0,-1).\end{cases}$$

The marching formula (10) is valid for all cells and, in particular, for the boundary cells. The no-slip boundary condition is enforced by automatically setting the boundary fluxes to zero.

As numerical flux, we choose the *local* Lax-Friedrichs flux, which is defined as

$$\begin{aligned}\boldsymbol{f}\big(\boldsymbol{u}_{K^\ell}^{n},\boldsymbol{u}_{L^\ell}^{n};\bar{\boldsymbol{x}}\big)&=\frac{\boldsymbol{f}\big(\boldsymbol{u}_{K^\ell}^{n};\bar{\boldsymbol{x}}\big)+\boldsymbol{f}\big(\boldsymbol{u}_{L^\ell}^{n};\bar{\boldsymbol{x}}\big)}{2}-\frac{a^{\mathrm{x}}(K^\ell,L^\ell)}{2}(\boldsymbol{u}_{K^\ell}^{n}-\boldsymbol{u}_{L^\ell}^{n}),\\ \boldsymbol{g}\big(\boldsymbol{u}_{K^\ell}^{n},\boldsymbol{u}_{L^\ell}^{n};\bar{\boldsymbol{x}}\big)&=\frac{\boldsymbol{g}\big(\boldsymbol{u}_{K^\ell}^{n};\bar{\boldsymbol{x}}\big)+\boldsymbol{g}\big(\boldsymbol{u}_{L^\ell}^{n};\bar{\boldsymbol{x}}\big)}{2}-\frac{a^{\mathrm{y}}(K^\ell,L^\ell)}{2}(\boldsymbol{u}_{K^\ell}^{n}-\boldsymbol{u}_{L^\ell}^{n}),\end{aligned}$$

where we used the abbrevation $\bar{\boldsymbol{x}}=\bar{\boldsymbol{x}}(K^\ell,L^\ell)$. The *local* Lax-Friedrichs flux can be systematically derived as that numerical flux that corresponds to a central Godunov-type scheme [34]. It produces much less numerical viscosity than the classical Lax-Friedrichs flux. The coefficients $a^{\mathrm{x}},a^{\mathrm{y}}$ are determined as the maximum spectral

radius on the cell interface

$$a^{\mathrm{x}}(K^\ell, L^\ell) = \max\big(\varrho(f'(\boldsymbol{u}^n_{K^\ell})), \varrho(f'(\boldsymbol{u}^n_{L^\ell}))\big),$$
$$a^{\mathrm{y}}(K^\ell, L^\ell) = \max\big(\varrho(g'(\boldsymbol{u}^n_{K^\ell})), \varrho(g'(\boldsymbol{u}^n_{L^\ell}))\big),$$

or upper estimates of that radius; here, the flux Jacobians $f'(\boldsymbol{u}_{K^\ell})$, $g'(\boldsymbol{u}_{K^\ell})$ are evaluated for the solution value $\boldsymbol{u}_{K^\ell}$ and $\varrho(f'(\boldsymbol{u}_{K^\ell}))$, $\varrho(g'(\boldsymbol{u}_{K^\ell}))$ are the corresponding spectral radii. The point $\bar{\boldsymbol{x}}(K^\ell, L^\ell)$ is the position of the interface between the cells K^ℓ and L^ℓ. Splitting (8) and then inserting (6), we write the *local* Lax-Friedrichs numerical flux as

$$\boldsymbol{f}\big(\boldsymbol{u}^n_{K^\ell}, \boldsymbol{u}^n_{L^\ell}; \bar{\boldsymbol{x}}(K^\ell, L^\ell)\big) = \frac{\big(\boldsymbol{h}(\boldsymbol{u}^n_{K^\ell}) + \boldsymbol{h}(\boldsymbol{u}^n_{L^\ell})\big) \otimes \boldsymbol{d}^{\mathrm{x}}(\bar{\boldsymbol{x}})}{2} - \frac{a^{\mathrm{x}}(K^\ell, L^\ell)}{2}(\boldsymbol{u}^n_{K^\ell} - \boldsymbol{u}^n_{L^\ell})$$
$$= \frac{1}{2}\begin{pmatrix} a_1\Big(u^n_{K^\ell}V(\boldsymbol{u}^n_{K^\ell}) + u^n_{L^\ell}V(\boldsymbol{u}^n_{L^\ell})\Big)d^{\mathrm{x}}_1\big(\bar{\boldsymbol{x}}(K^\ell, L^\ell)\big) \\ a_2\Big(v^n_{K^\ell}V(\boldsymbol{u}^n_{K^\ell}) + v^n_{L^\ell}V(\boldsymbol{u}^n_{L^\ell})\Big)d^{\mathrm{x}}_2\big(\bar{\boldsymbol{x}}(K^\ell, L^\ell)\big) \end{pmatrix} - \frac{a^{\mathrm{x}}(K^\ell, L^\ell)}{2}(\boldsymbol{u}^n_{K^\ell} - \boldsymbol{u}^n_{L^\ell}),$$

$$\boldsymbol{g}\big(\boldsymbol{u}^n_{K^\ell}, \boldsymbol{u}^n_{L^\ell}; \bar{\boldsymbol{x}}(K^\ell, L^\ell)\big) = \frac{\big(\boldsymbol{h}(\boldsymbol{u}^n_{K^\ell}) + \boldsymbol{h}(\boldsymbol{u}^n_{L^\ell})\big) \otimes \boldsymbol{d}^{\mathrm{y}}(\bar{\boldsymbol{x}})}{2} - \frac{a^{\mathrm{y}}(K^\ell, L^\ell)}{2}(\boldsymbol{u}^n_{K^\ell} - \boldsymbol{u}^n_{L^\ell})$$
$$= \frac{1}{2}\begin{pmatrix} a_1\Big(u^n_{K^\ell}V(\boldsymbol{u}^n_{K^\ell}) + u^n_{L^\ell}V(\boldsymbol{u}^n_{L^\ell})\Big)d^{\mathrm{y}}_1\big(\bar{\boldsymbol{x}}(K^\ell, L^\ell)\big) \\ a_2\Big(v^n_{K^\ell}V(\boldsymbol{u}^n_{K^\ell}) + v^n_{L^\ell}V(\boldsymbol{u}^n_{L^\ell})\Big)d^{\mathrm{y}}_2\big(\bar{\boldsymbol{x}}(K^\ell, L^\ell)\big) \end{pmatrix} - \frac{a^{\mathrm{y}}(K^\ell, L^\ell)}{2}(\boldsymbol{u}^n_{K^\ell} - \boldsymbol{u}^n_{L^\ell}).$$

The spectral radii for the coefficients $a^{\mathrm{x}}(K^\ell, L^\ell)a^{\mathrm{y}}(K^\ell, L^\ell)$, are estimated as

$$a^{\mathrm{x}}(K^\ell, L^\ell) = \max\big(a_1, a_2\big)\max\Big(V(\boldsymbol{u}^n_{K^\ell})d^{\mathrm{x}}_1\big(\bar{\boldsymbol{x}}(K^\ell, L^\ell)\big), V(\boldsymbol{u}^n_{L^\ell})d^{\mathrm{x}}_2\big(\bar{\boldsymbol{x}}(K^\ell, L^\ell)\big)\Big),$$
$$a^{\mathrm{y}}(K^\ell, L^\ell) = \max\big(a_1, a_2\big)\max\Big(V(\boldsymbol{u}^n_{K^\ell})d^{\mathrm{y}}_1\big(\bar{\boldsymbol{x}}(K^\ell, L^\ell)\big), V(\boldsymbol{u}^n_{L^\ell})d^{\mathrm{y}}_2\big(\bar{\boldsymbol{x}}(K^\ell, L^\ell)\big)\Big).$$

4.2. **Multiresolution setting.** The success of the multiresolution algorithm depends strongly on a coarse representation of the solution plus a sequence of details that contain information about the differences between two consecutive resolution levels. This information is related to the regularity of the solution (see e.g. [38]). For $x \in K^\ell$, let $\tilde{\varphi}_{K^\ell}(x) := |K^\ell|^{-1}\chi_{K^\ell}(x)$, where χ_{K^ℓ} is the characteristic function of K^ℓ. This allows us to write the average of u over the cell K^ℓ as $u_{K^\ell} := \big(u, \tilde{\varphi}_{K^\ell}\big)_{L^1(\Omega)}$.

For the navigation between resolution levels, certain adequate transfer operators are needed. These allow us to determine an invertible transformation between finite volumes on level $\ell = H$, and the set formed by finite volumes on the coarsest level $\ell = 0$ and a sequence of so-called wavelet coefficients. To switch from fine to coarser levels, a *projection* or coarsening operator is defined by

$$u_{K^\ell} = \sum_{L^{\ell+1}_i \in \mathcal{M}_{K^\ell}} \frac{|L^{\ell+1}_i|}{|K^\ell|} u_{L^{\ell+1}_i}, \quad \tilde{\varphi}_{K^\ell} = \sum_{L^{\ell+1}_i \in \mathcal{M}_{K^\ell}} \frac{|L^{\ell+1}_i|}{|K^\ell|} \tilde{\varphi}_{L^{\ell+1}_i},$$

where $\mathcal{M}_{K^\ell}$ stands for the refinement set of the control volume K^ℓ, whose four elements are control volumes, contained in the spatial position occupied by K^ℓ, that belong to $\mathcal{T}^{\ell+1}$. To move from coarse to finer levels, a *prediction* operator is employed.

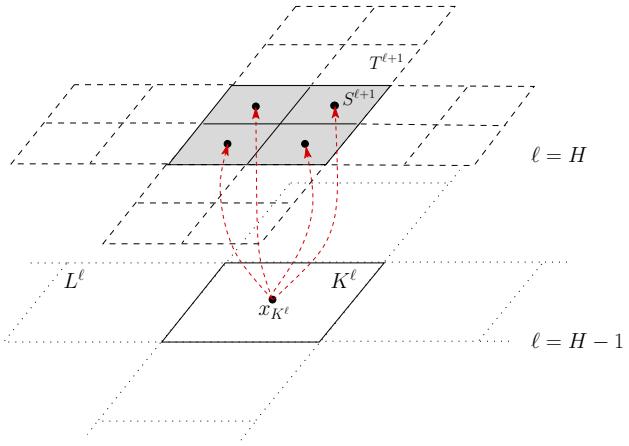

FIGURE 1. Sketch of a graded tree structure. Here K^ℓ is a parent node on level $\ell = H-1$, its children nodes (including $S^{\ell+1}$) belong to $\mathcal{L}(\Lambda)$; L^ℓ is a virtual node and $T^{\ell+1}$ is a virtual leaf.

As in [12], we choose this to be the following polynomial reconstruction:

$$\tilde{u}_{K^{\ell+1}} = u_{T^\ell} - \sum_{m=1}^{s} \tilde{\gamma}_m \left[\left(u_{S^\ell_x} - u_{S^\ell_{-x}} \right) + \left(u_{S^\ell_x} - u_{S^\ell_{-x}} \right) \right] + \sum_{m=1}^{s} \tilde{\gamma}_m \sum_{p=1}^{s} \tilde{\gamma}_p \left(u_{S^\ell_{xy}} - u_{S^\ell_{x,-y}} - u_{S^\ell_{-x,y}} + u_{S^\ell_{-x-y}} \right),$$

where $\tilde{\gamma}_1 = -22/128$, $\tilde{\gamma}_2 = 3/28$ are prediction coefficients. The *wavelet* function for $x \in K^{\ell+1}$ is

$$\tilde{\psi}_{K^\ell,j} = \tilde{\varphi}_{L_i^{\ell+1}} - \sum_{m=-s}^{s} \tilde{\gamma}_{i+m} \tilde{\varphi}_{L^l_{i+m}} \quad \text{for } j = 1, \dots, 4,$$

where $L_i^{\ell+1} \in \mathcal{M}_{K^\ell}$. The error induced by the prediction operator at the finite volume K^ℓ is defined as the difference between the cell average and the predicted value, i.e., $d^u_{K^\ell} := u_{K^\ell} - \tilde{u}_{K^\ell}$. It follows from the definition of the wavelet function that $d^u_{K^\ell} = \left(u, \tilde{\psi}_{K^\ell}\right)_{L^1(\Omega)}$. If u is sufficiently smooth, its wavelet coefficients decrease when going from coarser to finer levels. Thus, the compression of data by discarding the information corresponding to small wavelet coefficients, or *thresholding* procedure, is automatically achieved. In practice, the algorithm consists in discarding all control volumes corresponding to wavelet coefficients for which

$$\left| d^u_{K^\ell} \right| < \varepsilon_\ell, \quad \ell = 0, \dots, H$$

where ε_ℓ is a level-dependent tolerance. Given a reference tolerance ε_{R} whose choice depends on the maximum values of the reaction and diffusion coefficients, we can determine ε_ℓ by

$$\varepsilon_\ell = 2^{2(\ell - H)} \varepsilon_{\mathrm{R}}, \quad \ell = 0, \dots, H.$$

These level-dependent tolerances guarantee that the error due to thresholding is of the same order as the discretization error, and therefore the order of the underlying scheme is preserved. For multi-species problems, wavelet coefficients will be defined

by $\boldsymbol{d}_{K^\ell} = \min\left\{\left|d^u_{K^\ell}\right|, \left|d^v_{K^\ell}\right|\right\}$ and $\boldsymbol{d}_{K^\ell} = \max\left\{\left|d^u_{K^\ell}\right|, \left|d^v_{K^\ell}\right|\right\}$ for the refinement and coarsening procedures, respectively.

4.3. **Dynamic tree structure and measures of compression.** Two core ingredients of the fully adaptive multiresolution framework are the *graded tree* data storage and an efficient procedure to navigate inside it (see Figure 1). The *root* is the basis of the tree. A parent node has four children, and the children of the same parent are called *brothers*. A node without children is a *leaf*. A given node has $s' = 2$ *nearest neighbors* in each spatial direction. These are needed for the computation of the fluxes of leaves. If these neighbors do not exist, we create them as *virtual leaves*. We denote by Λ the set of all nodes of the tree, by $\mathcal{L}(\Lambda)$ the restriction of Λ to the leaves, and by $\mathcal{L}(\Lambda^\ell)$ the restriction of $\mathcal{L}(\Lambda)$ to the level ℓ for $\ell = 0, \ldots, H$. Once the thresholding is done, we add a *safety zone* to the tree, by adding one finer level to all the leaves in the tree without violating the graded-tree data structure. This is a crucial point because it eliminates the need to decode the solution back to the finest resolution level at each time step. In addition, to enforce conservation in the scheme, we compute only the fluxes at level $\ell + 1$ and set the ingoing flux on the leaf at level l equal to the sum of the outgoing fluxes on the leaves of level $\ell + 1$ sharing the same edge. Notice that the marching formula (10) in the adaptive scheme is used not for all $K^\ell \in \Lambda^\ell$ but only for each $K^\ell \in \mathcal{L}(\Lambda^\ell)$, $\ell = 0, \ldots, H$.

The quantity $\eta := \mathcal{N}/(2^{-2H}\mathcal{N} + \#\mathcal{L}(\Lambda))$, called the *data-compression rate* [22], is used to measure the improvement in data compression. Here, $\mathcal{N}$ is the number of control volumes in the full finest grid at level $\ell = H$, and $\#\mathcal{L}(\Lambda)$ is the number of leaves in the tree. The *speed-up* $\mathcal{V}$ between the CPU times of the numerical solutions (obtained by the one-level finite-volume method and the fully adaptive multiresolution method) is defined by $\mathcal{V} := \text{CPU time}_{\text{FV}}/\text{CPU time}_{\text{MR}}$.

The multiresolution setting allows us to accurately resolve the solution at the sharp interfaces which originate from pattern formation, where the patterns correspond to separated pedestrian groups.

5. **Numerical examples.** In the numerical examples, the convection coefficients are normalized to $a_1 = a_2 = 1$. The diffusion matrix is assumed to be constant taking the form

$$\mathbf{b}(\boldsymbol{u}) = \begin{pmatrix} \varepsilon & \delta \\ \delta & \varepsilon \end{pmatrix} \tag{11}$$

with self-diffusion rate ε and cross-diffusion rate δ. The cross-diffusion rate δ is assumed to vanish in all examples, except the last one (Example 7). If not otherwise specified, in the numerical examples we set the velocity function to $V(u, v) = 1 - u - v$, the domain to $\Omega = [-1, 1]^2$, and on the boundary we impose absorbing boundary conditions.

5.1. **Example 1: Flow towards exit targets.** In Example 1 a perpendicular flow towards exit targets is considered. Two different populations are supposed to cross in the center of the square-shaped domain $\Omega = [-1, 1] \times [-1, 1]$, where their streams are supposed to intersect. To enforce this intersection, the entries of the populations are situated in two adjacent corners, and their exits are in the respective opposite corners, mirrored by the origin. At the beginning of the simulation, the domain is assumed to be empty, i.e. the initial data are set to $(0, 0)$ all over the domain Ω. The two populations enter the domain through doors of width w, which for the test

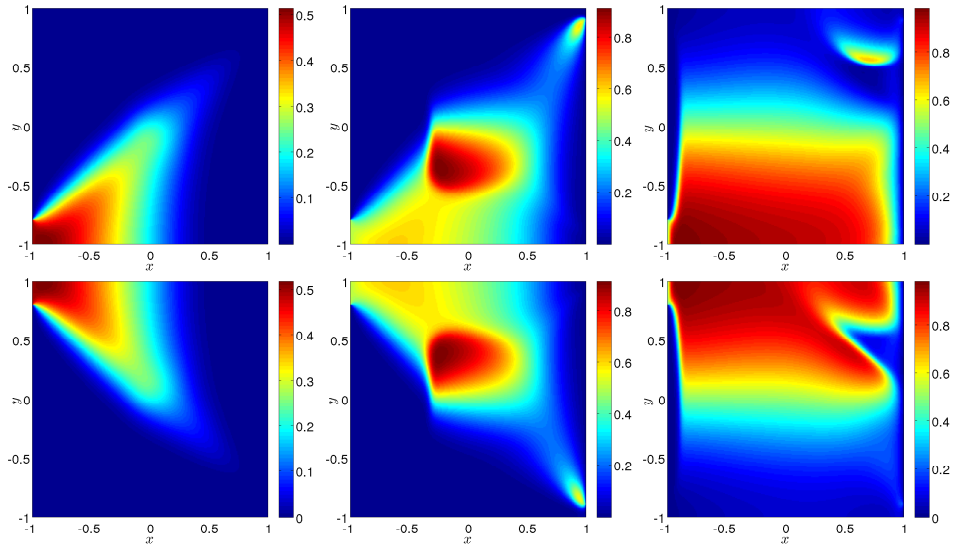

FIGURE 2. Example 1. Species' densities u (top) and v (bottom) at times $t = 2.0$, $t = 4.0$, and $t = 18.0$.

case is specified to be $w = 0.1$. The two inlets are positioned at $\{-1\} \times [-1, -1+w]$ and $\{-1\} \times [1-w, 1]$ for the populations quantified by u and v, respectively. The entrance flow is specified by Neumann boundary conditions that quantify the fluxes at the inlets; the entrance fluxes are defined as

$$f_1(\boldsymbol{u}; \boldsymbol{x}) = f_{\mathrm{SW}} \quad \text{for} \quad \boldsymbol{x} \in \{-1\} \times [-1, -1+w],$$
$$f_2(\boldsymbol{u}; \boldsymbol{x}) = f_{\mathrm{NW}} \quad \text{for} \quad \boldsymbol{x} \in \{-1\} \times [1-w, 1],$$

with $f_{\mathrm{NW}} = f_{\mathrm{SW}} = 0.5$. The exit fluxes are defined at the outlets $\{1\} \times [1-w, 1]$ and $\{1\} \times [-1, -1+w]$ as

$$f_1(\boldsymbol{u}; \boldsymbol{x}) = up, \ f_2(\boldsymbol{u}; \boldsymbol{x}) = 0 \quad \text{for} \quad \boldsymbol{x} \in \{1\} \times [-1, -1+w],$$
$$f_2(\boldsymbol{u}; \boldsymbol{x}) = vq, \ f_1(\boldsymbol{u}; \boldsymbol{x}) = 0, \quad \text{for} \quad \boldsymbol{x} \in \{1\} \times [1-w, 1],$$

with $p = q = 1$. The remaining parameters are set to $a_1 = a_2 = 1$, $\varepsilon = 0.01$, $\delta = 0$.

The crowd dynamics are oriented towards exit targets for both populations. The targets are located in the centers of the respective exit doors and are located at $(x_1, y_1) = (1, 1-w/2)$, $(x_2, y_2) = (1, -1+w/2)$. The directions towards the targets (exit points) (x_1, y_1), (x_2, y_2) for species 1 and 2, respectively, are given by

$$\boldsymbol{d}_i(\boldsymbol{x}) = \frac{\tilde{\boldsymbol{d}}_i(\boldsymbol{x})}{\|\tilde{\boldsymbol{d}}_i(\boldsymbol{x})\|_2}, \quad \tilde{\boldsymbol{d}}_i(\boldsymbol{x}) = \begin{pmatrix} x - x_i & y - y_i \end{pmatrix}, \qquad i = 1, 2.$$

Therefore, the pedestrian flow is directed towards a location-dependent direction. In Figure 2 one recognizes the first pedestrians reaching the opposite corner avoiding the jam. Thereafter the flow towards the opposite corners does not continue but slowly a big jam in the center is built up. The two big clusters, one for each population, block each other, letting only the small early fractions cross towards the outlets. Even though the states obtained during the simulation are inside the elliptic region, there is no phase separation. This means that data getting inside an elliptic region does not necessarily cause pattern formation. It can be conjectured,

however, that phase separation and pattern formation can be obtained for certain changes in the boundary conditions.

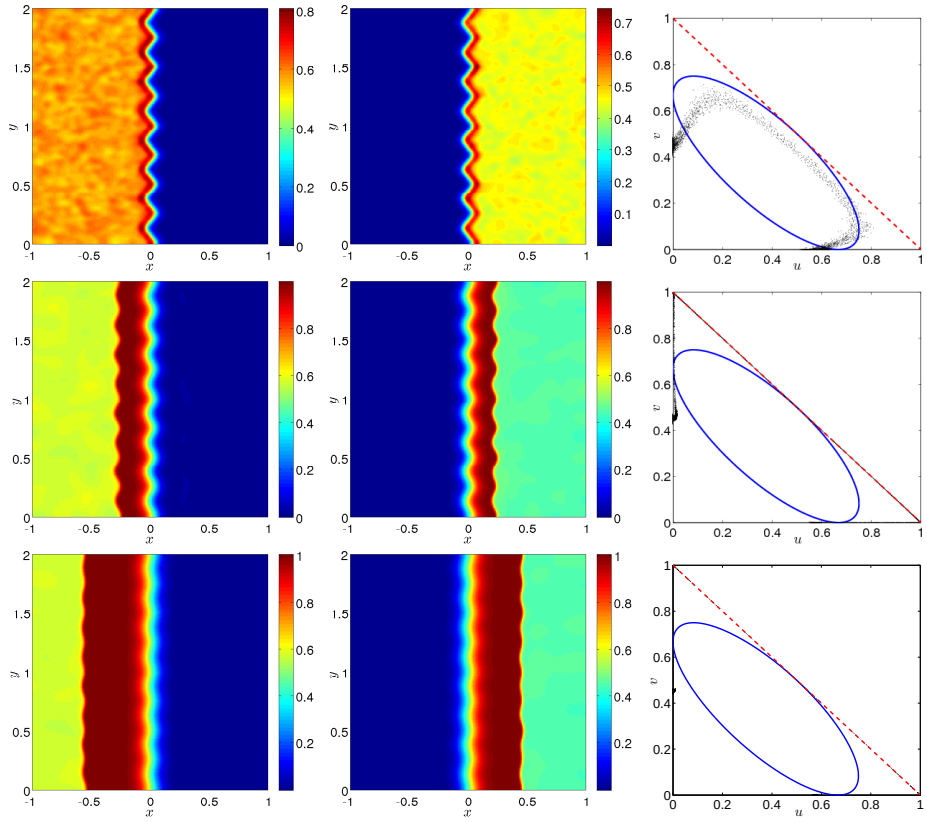

FIGURE 3. Example 2. Species' densities u (left), v (right), and corresponding phase diagram where the elliptic region is depicted, for times $t = 0.1$ (top), $t = 0.5$ (center) and $t = 1.5$ (bottom).

5.2. **Example 2: Battle of Agincourt.** Example 2 gives an account of the Battle of Agincourt, 1415, a relatively well documented medieval war. In [17], the historical setting is recalled and related to a pedestrian model framework, but no numerical simulations are performed. The flow is assumed to be in opposite directions, i.e. we set

$$\boldsymbol{d}_1(\boldsymbol{x}) = \begin{pmatrix} 1 & 0 \end{pmatrix}, \quad \boldsymbol{d}_2(\boldsymbol{x}) = \begin{pmatrix} -1 & 0 \end{pmatrix}.$$

In this case of this countercurrent flow, system (4) can be specified as

$$u_t + \big(u(1-u-v)\big)_x = \varepsilon \Delta u, \qquad v_t - \big(v(1-u-v)\big)_x = \varepsilon \Delta v.$$

The boundary conditions are absorbing.

An idealized battle model would initially set the two opposed armies at opposite sides of a field. Therefore, in the initial conditions the two phases are separated in two parts, in each of which only one phase is present and the other not. Tentative simulations with a straight interface between both armies, where a straight line in

the center separates both phases, did not lead to pattern formation, even if the initial values at each side are perturbed. Therefore, a serrated interface in form of a zig-zag curve with frequency F and amplitude A is assumed. More specifically, introducing the zig-zag curve

$$z(y) = 4A\left(\left|Fy - \lfloor Fy \rfloor - \frac{1}{2}\right| - \frac{1}{4}\right),$$

where $\lfloor\cdot\rfloor$ indicates the next lower integer, the domain is divided into two parts as

$$\Omega_u = \{-1 \le x \le z(y),\ 0 \le y \le 2\}, \quad \Omega_v = \{z(y) < x \le 1,\ 0 \le y \le 2\},$$
$$\Omega = \Omega_u \cup \Omega_v = [-1, 1] \times [0, 2].$$

For amplitude $A = 0$ the interface corresponds to a straight line. In the examples we choose $A = 0.05$ and $F = 4$. The initial conditions are

$$u(\boldsymbol{x}, t = 0) = u_0 + \eta_u(\boldsymbol{x}), \quad v(\boldsymbol{x}, t = 0) = 0 \quad \text{if} \quad \boldsymbol{x} \in \Omega_u,$$
$$v(\boldsymbol{x}, t = 0) = 0, \quad v(\boldsymbol{x}, t = 0) = v_0 + \eta_v(\boldsymbol{x}) \quad \text{if} \quad \boldsymbol{x} \in \Omega_v,$$

where $u_0 = v_0 = 0.2$ and η_u, η_v are uniformly distributed random noise with variations of 10% and 1.5% for u and v, respectively. For the multiresolution setting, $L = 10$ resolution levels are used with a reference tolerance of $\varepsilon_{\text{ref}} = 1.25 \times 10^{-3}$.

In Figure 3, a positive amplitude $A > 0$ was intended to enforce some pattern formation through an interface boundary perturbation, but obviously such an interface perturbation has the effect of an interface boundary regularization, keeping the essentially one-dimensional solution structure. In a similar but one-dimensional setting, where two initially separated opposed phases of solid material dispersed in a liquid move towards each other and the vector-valued flux function provides an elliptic region, the same locking effect could be observed [5]. This locking effect is not changed in a two dimensional setting, at least for a standard parameter setting.

5.3. **Example 3: Countercurrent flow in a long channel.** In Example 3, the domain is specified to be a long channel having the domain $\Omega = [-5, 5] \times [-1, 1]$. The parameters are set to $a_1 = a_2 = 1$, $\varepsilon = 2.5 \times 10^{-3}$, $\delta = 0$. Initially, the domain is assumed to be empty with $u(\boldsymbol{x}, t = 0) = v(\boldsymbol{x}, t = 0) = 0$ for all $\boldsymbol{x} \in \Omega$. Both populations move in opposite directions

$$\boldsymbol{d}_1(\boldsymbol{x}) = \begin{pmatrix} 1 & 0 \end{pmatrix}, \quad \boldsymbol{d}_2(\boldsymbol{x}) = \begin{pmatrix} -1 & 0 \end{pmatrix},$$

such that they are expected to meet somewhere in the middle. The two populations access the domain at two opposite edges; at the left and right edges of the domain, an inflow is imposed:

$$\boldsymbol{f}(\boldsymbol{u}, \boldsymbol{x}) - \varepsilon \partial_x \boldsymbol{u} = \begin{pmatrix} f_{\text{W}}(t) & 0 \end{pmatrix}^{\text{T}} \quad \text{at} \quad \boldsymbol{x} \in \{-5\} \times [-1, 1],$$
$$\boldsymbol{f}(\boldsymbol{u}, \boldsymbol{x}) - \varepsilon \partial_x \boldsymbol{u} = \begin{pmatrix} 0 & f_{\text{E}}(t) \end{pmatrix}^{\text{T}} \quad \text{at} \quad \boldsymbol{x} \in \{5\} \times [-1, 1].$$

The boundaries of the longer edges are assigned with zero flux, i.e.,

$$\boldsymbol{g}(\boldsymbol{u}; \boldsymbol{x}) - \varepsilon \partial_y \boldsymbol{u} = \boldsymbol{0}, \quad \boldsymbol{x} \in [-5, 5] \times \{-1, 1\}.$$

The populations finally leave the domain with a constant rate at the respective target side

$$\boldsymbol{f}(\boldsymbol{u}, \boldsymbol{x}) - \varepsilon \partial_x \boldsymbol{u} = -\boldsymbol{u} \quad \text{at} \quad \boldsymbol{x} \in \{-5, 5\} \times [-1, 1].$$

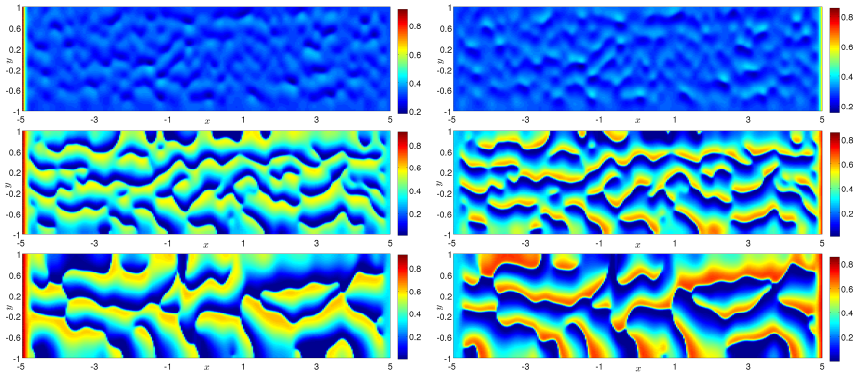

FIGURE 4. Example 3. Species' densities u, v at times $t = 2$, $t = 4$, $t = 8$.

In Figure 4, a strong spatial phase-separation can be recognized, which becomes more distinct with time. The patterns are oriented in the direction of the countercurrent flow. This corresponds to the intuition on crowds, in which all pedestrians prefer to move alongside their own peers in the same channel in order to avoid collisions. This separation is caused by data entering the elliptic region in the phase space. The instability of states in the elliptic region makes them leave it, which leads to channel formation. The patterns are alongside (parallel) to the flow direction, i.e. the phases move through their respective channels. The phenomenon of pattern formation and its relation to the elliptic region is studied further in the following examples.

5.4. **Example 4: Countercurrent flow.** In Example 4, countercurrent flow is modelled, where two groups of pedestrians move in the opposite directions $\boldsymbol{d}_1(\boldsymbol{x}) = (0,1)$ and $\boldsymbol{d}_2(\boldsymbol{x}) = (0,-1)$. Inside the domain $\Omega = [-1,1]^2$, the initial data are set to be randomly perturbed around a state $\boldsymbol{u}_0 = (0.4, 0.35)^{\mathrm{T}}$ which is located inside the elliptic region. More specifically, initial conditions are set to

$$u(\boldsymbol{x}, t=0) = u_0 + \eta_u(\boldsymbol{x}), \quad v(\boldsymbol{x}, t=0) = v_0 + \eta_v(\boldsymbol{x}), \quad \text{for} \quad \boldsymbol{x} \in \Omega = [-1,1]^2, \tag{12}$$

where η_u, η_v are uniformly distributed random noise with variations of 10% and 1.5% for u and v, respectively. The boundary conditions are set to be absorbing. Here the diffusion matrix has the values $\varepsilon = 1.5 \times 10^{-3}$, whereas $\delta = 0$. For the multiresolution setting, $L = 10$ resolution levels are used with a reference tolerance of $\varepsilon_{\mathrm{ref}} = 1.25 \times 10^{-2}$.

As one can see in Figure 5, a clear and strong spatial phase-separation is confirmed for initial data inside the elliptic region. This separation leads to channel formation, where the phases separate horizontally and move through vertical channels. Moreover, clusters with a predominant species, moving in the directions of that species, are formed. For initial data $\boldsymbol{u}_0$ chosen outside the elliptic region, the variation of the density values remains very low and close to the initial state and therefore remains clearly outside the elliptic region.

5.5. **Example 5: Perpendicular flow with different velocity functions.** In Example 5, a crossing with perpendicular flow directions $\boldsymbol{d}_1(\boldsymbol{x}) = (1,0)$, $\boldsymbol{d}_2(\boldsymbol{x}) = (0,1)$ is considered in the domain $\Omega = [-1,1]^2$. Self-diffusion and cross-diffusion

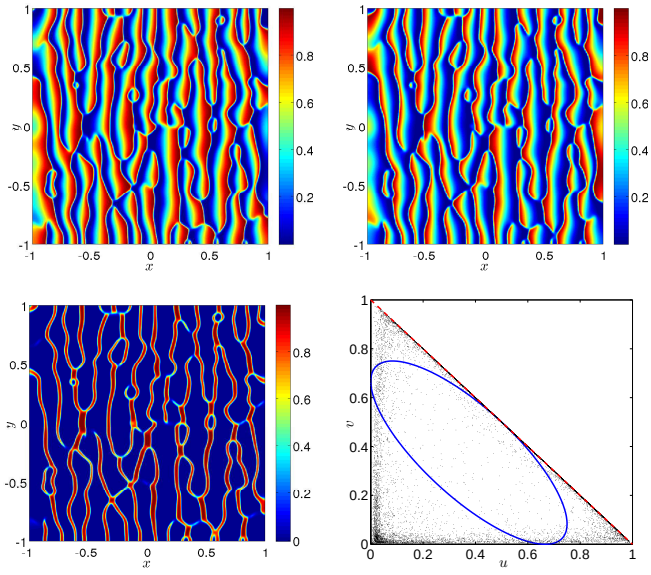

FIGURE 5. Example 4. Species' densities u, v (top), void fraction $1-u-v$ (bottom-left), and corresponding phase diagram where the elliptic region is depicted (bottom-right). The simulated time is $t = 2$.

are set to $\varepsilon = 1 \times 10^{-3}$, $\delta = 0$, respectively. As in Example 4, there are absorbing boundary conditions and homogeneous initial data (12) with $\boldsymbol{u}_0 = (0.4, 0.35)^{\mathrm{T}}$ are taken inside the elliptic region. Moreover, we consider different velocity functions which are intended to describe real and hypothesized forces during interactions between pedestrians. The velocity function $V(u,v) = 1-u-v$ assumes a slow-down that is proportional to $u+v$. This choice falls in the more general class of velocity functions that have the desirable property that $V(u,v)$ is convex and satisfies

$$V(0,0) = 1, \quad V(1,0) = 0, \quad V(0,1) = 0. \tag{13}$$

This property is also satisfied for $V(u,v) = (1-u-v)(1-u)(1-v)$, which has a wider elliptic region, and for $V(u,v) = 1-u-v-uv$, where the elliptic region is thinner; this thinner elliptic region coincides with an overall smaller invariant region, in comparison to our standard setting. Clearly $1-u-v-uv < 1-u-v$ for $u, v > 0$. Such a reduced invariance region corresponds to the interpretation that in a dense packing there is some space between pedestrians, in particular if they belong to different groups moving in different directions.

The flow patterns corresponding to these velocity functions can be seen in Figure 6. The perpendicular flow results in the formation of diagonal patterns. For the velocity functions $V(u,v) = 1-u-v$ and $V(u,v) = 1-u-v-uv$, the solution values are dispersed throughout the invariance region. For the velocity function $V(u,v) = (1-u-v)(1-u)(1-v)$ the solution values are concentrated in a bold subregion of the elliptic region; there is no solution value outside this subregion. For the velocity function $V(u,v) = 1-u-v-uv$, there is an accumulation of solution values at the maximum packing line, in particular at its tangent to the

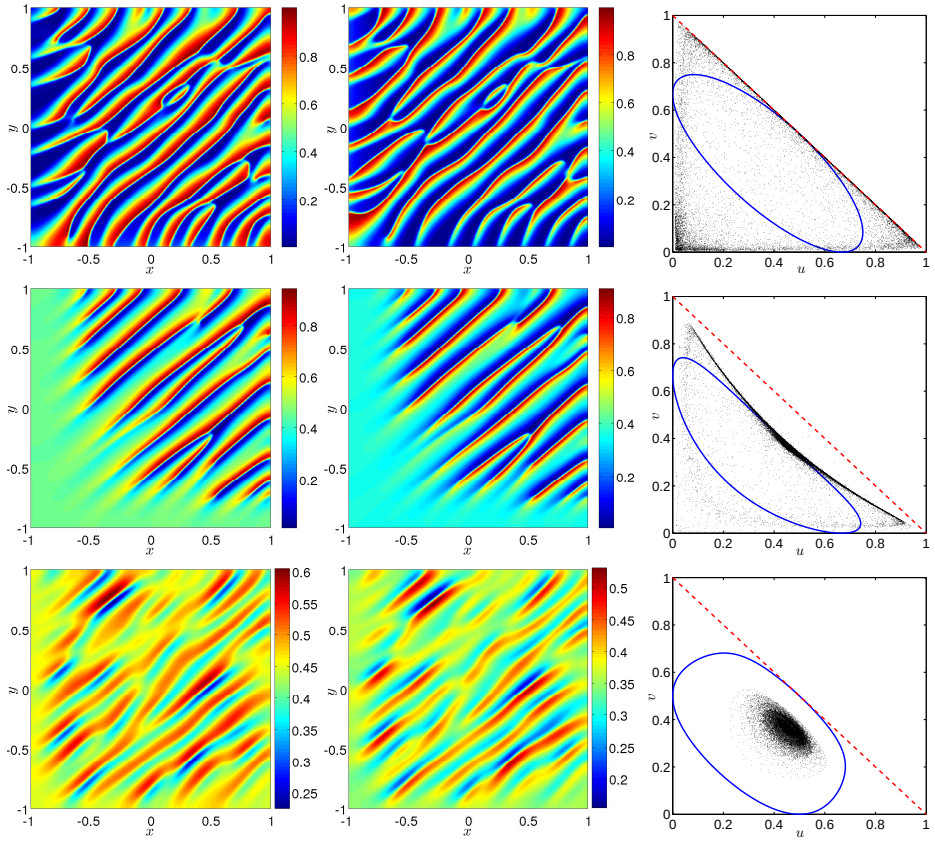

FIGURE 6. Example 5. Species' densities u, v, and phase diagrams at the final time $t = 2.5$ for different velocities $V(u, v)$. Top: $V(u, v) = 1 - u - v$, middle: $V(u, v) = 1 - u - v - uv$, and bottom: $V(u, v) = (1 - u)(1 - v)(1 - u - v)$.

elliptic region. The variant $V(u, v) = 1 - \max(u, v)$ is convex (even if not strictly convex) and satisfies (13) but allows a superposition of different pedestrians types, since the boundary of the invariant region is $\max(u, v)$, which contains a value like $(u, v) = (1, 1)$. Moreover, there is no elliptic region, and thus the interesting feature of pattern formation cannot be obtained.

5.6. **Example 6: Effect of diffusion and cross-diffusion.** In Example 6 the effects of the self-diffusion (which is represented by the parameter ε) and in particular of the cross-diffusion (represented by parameter δ) in the constant diffusion matrix (11) are examined. We take the same setting as in Example 4 on the countercurrent flow, but additionally consider the parameter δ in the off-diagonal entries of the diffusion matrix, i.e., δ accounts for the intensity of the cross-diffusion. In particular, we choose $\varepsilon \in \{0, 0.001, 0.01, 0.1\}$ and $\delta \in \{0, 0.01, 1, 2.5, 5, 10\}$. In all cases of the test series, it can be seen that a small self-diffusion is necessary in order to ensure stability of the numerical scheme, see Table 1. Figure 7 displays snapshots at $t = 2.0$ for $\varepsilon = 0.01$ and several choices of δ. First, one observes that from $\delta \geq 1$ directed patterns become clearly detectable and the width of the channels increases

with δ. For $\delta < 1$ the patterns eventually smooth out to the equilibrium state. For a certain parameter range, the cross-diffusion leads to more uniform shape of the channels.

TABLE 1. Example 7. Behavior of the numerical solution depending on the diffusion and cross-diffusion parameters ε and δ.

ε	δ	Unstable	Stable patterns	Steep patterns
0	0, 0.01, 1, 2.5, 5, 10	•		
0.001	0, 1		•	
0.001	1.5, 2.5			•
0.001	5, 10	•		
0.01	0, 0.01, 0.1		•	
0.01	1, 2.5, 5, 10			•
0.1	0, 0.01, 0.1		•	
0.1	1, 2.5, 5, 10	•		

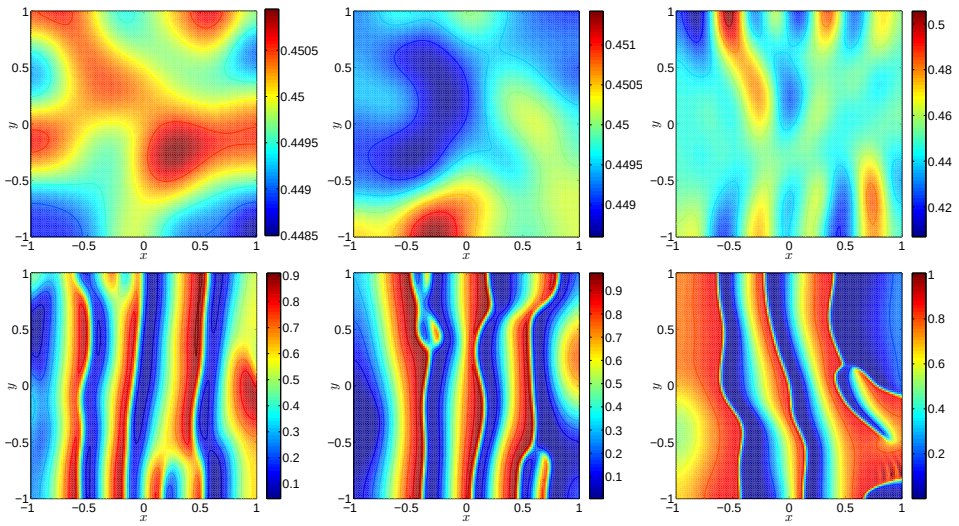

FIGURE 7. Example 6. Densities for species u at time $t = 2.0$. Here, $\varepsilon = 0.01$, and, from top-left, $\delta \in \{0, 0.01, 1, 2.5, 5, 10\}$.

6. **Conclusion and future research.** We have examined a generic two-dimensional multiphase extension of the scalar LWR model and found several interesting features. Unlike highway traffic flow in which opposing streams are separated or meet only at intersection points, pedestrian flow in buildings or open spaces allows for direct interaction between flows in opposite directions or at right angles. The particular feature of the presented model is that it considers both two space dimensions and two different pedestrian types. Test scenarios can be handled by using a finite-volume-multiresolution algorithm.

A genuine setting for the presented model is that of a crossing, where two different pedestrian types cross a place in perpendicular directions. The simulation of pedestrian flow where the two groups cross in the middle of the domain leads to jamming. This mutual blocking of two different phases is not caused by a wall or an obstacle, but by the crossing flow direction where two phases meet at a high pedestrian density. A simplified simulation of the Battle of Agincourt, where two opposed armies move towards each other, also leads to such a blocking, even when the initial data and the initial interface between the armies are perturbed. The considered simulation model allows flow towards exit targets, where certain boundary conditions correspond to entries and exits. A simulation of countercurrent flow in a long channel, where two pedestrian phases enter from opposite edges and move towards each other, leads to a strong spatial phase-separation that becomes more distinct with time. In the case that homogeneous initial data are chosen, with an initial state inside the elliptic region, a steep pattern formation is generated. If the flows are countercurrent, the pattern is parallel to the flow direction. If the flows are perpendicular, the pattern is diagonal, suggesting that the flow direction is diagonal. The form of the velocity function impacts the shape of the pattern. A test series with different values for the diffusion matrix shows that a small diffusion term is necessary to stabilize the simulation, whereas the cross-diffusion term can account in a certain range for steeper patterns.

These examples show that the model is able to reproduce some phenomena of interest, and that the multiresolution algorithm is an adequate tool for the solution of two-dimensional problems in pedestrian flow, in particular when the pattern formation demands high refinements at the phase interfaces.

From a mathematical point of view, an open topic is the existence and uniqueness of the equations of hyperbolic-elliptic degenerate type, which need to be analyzed in the context of measure-valued solutions. Elliptic degeneracy implies that the solution of Riemann problems in the hodograph plane requires completely new techniques such as complex characteristics.

From an applications point of view, our approach is principally well suited for the modeling of distinct pedestrian streams. Obviously, it can be extended to more complicated, realistic geometries, and to more than two phases. The model avoids the problems arising in the context of necessary momentum conservation in Euler-/Navier-Stokes based approaches and, other than [16, 40] , e.g., the density remains limited from above.

The examples, in particular Example 1, illustrate, however, the limitations of the purely macroscopic approach which have to be overcome in the future development of the simulation model. In Example 1, smaller groups of pedestrians are able to reach their exit doors as long as the densities in the crossing area are still small. With increasing densities a jam occurs first in the crossing area and leads finally to a blocking at the horizontal center line of the region. This effect is also a result of diffusion created by the Laplace term. The situation of the model can be illustrated by the comparison with blind persons knowing their destination, following strictly their direction and searching for their path using their canes. When encountering a high concentration of other pedestrians, they stop. The diffusion term enables them to sidestep, but only slightly, and usually they will not find the right way to their destination again. Numerically, small diffusion facilitates slight movement in the presence of high densities, but a higher diffusion rate would spread the particles

(pedestrians) much wider in the region in contrast to the intended modeling of a target-oriented movement of distinct streams.

Pedestrians either tend to pass across a jam directly as long as possible or to circumvent it for resuming their way to their final destination. In order to model this behavior, an additional strategy will be needed. One possibility could be to let the pedestrians walk along graphs which describe possible paths from the current position which are restricted by visibility. We will adopt another approach by introducing adaptable potential fields where pedestrians are guided to their target using potential lines. A similar approach has been used in [16, 40].

Another problem results from the fact that pedestrians have, unlike gas or fluid molecules, a non-negligible physical extent and an individual behavior: The analogy to flow models is limited to high densities where both aspects do not predominate. As long as densities are small enough to give sufficient space for (individual) movement, there is a need for modeling local interaction of pedestrians. We intend, therefore, to complement the model by an adequate microscopic component based on discrete structures.

Acknowledgments. The first author is supported by Conicyt (Chile) through the Fondecyt project #11080253. The work of the second author is supported by the European Research Council Advanced Grant "Mathcard, Mathematical Modeling and Simulation of the Cardiovascular System", Project ERC-2008-AdG 227058 and by the postdoctoral program "Becas Chile". The third author is supported by the Deutsche Forschungsgemeinschaft (German Research Foundation) through project SCHW548/5-1.

REFERENCES

[1] B. Andreianov, M. Bendahmane and R. Ruiz-Baier, *Analysis of a finite volume method for a cross-diffusion model in population dynamics*, Math. Models Meth. Appl. Sci., **21** (2011), 307–344.

[2] A.V. Azevedo, D. Marchesin, B. Plohr and K. Zumbrun, *Capillary instability in models for three-phase flow*, Z. Angew. Math. Phys., **53** (2002), 713–746.

[3] J. B. Bell, J. A. Trangenstein and G. R. Shubin, *Conservation laws of mixed type describing three-phase flows in porous media*, SIAM J. Appl. Math., **46** (1986), 1000–1017.

[4] S. Benzoni-Gavage and R. M. Colombo, *An n-populations model for traffic flow*, Eur. J. Appl. Math., **14** (2003), 587–612.

[5] S. Berres, R. Bürger and K. H. Karlsen, *Central schemes and systems of conservation laws with discontinuous coefficients modeling gravity separation of polydisperse suspensions*, J. Comput. Appl. Math., **164/165** (2004), 53–80.

[6] S. Berres, R. Bürger and A. Kozakevicius, *Numerical approximation of oscillatory solutions of hyperbolic-elliptic systems of conservation laws by multiresolution schemes*, Adv. Appl. Math. Mech., **1** (2009), 581–614.

[7] S. Berres and R. Ruiz-Baier, *A fully adaptive numerical approximation for a two-dimensional epidemic model with non-linear cross-diffusion*, Nonlin. Anal. Real World Appl., **12** (2011), 2888–2903.

[8] S. Berres, R. Ruiz-Baier, H. Schwandt and E. M. Tory, *Two-dimensional models of pedestrian flow*, in "Series in Contemporary Applied Mathematics" (Proceedings of HYP 2010) (eds. P. G. Ciarlet and Ta-Tsien Li), Higher Education Press, Beijing, World Scientific, Singapore, 2011, to appear.

[9] J. H. Bick and G. F. Newell, *A continuum model for two-directional traffic flow*, Quart. Appl. Math., **18** (1960), 191–204.

[10] L. Bruno, A. Tosin, P. Tricerri and F. Venuti, *Non-local first-order modelling of crowd dynamics: A multidimensional framework with applications*, Appl. Math. Model., **35** (2011), 426–445.

[11] R. Bürger, K. H. Karlsen, E. M. Tory and W. L. Wendland, *Model equations and instability regions for the sedimentation of polydisperse suspensions of spheres*, ZAMM Z. Angew. Math. Mech., **82** (2002), 699–722.
[12] R. Bürger, R. Ruiz-Baier and K. Schneider, *Adaptive multiresolution methods for the simulation of waves in excitable media*, J. Sci. Comput., **43** (2010), 261–290.
[13] C. Burstedde, K. Klauck, A. Schadschneider and J. Zittartz, *Simulation of pedestrian dynamics using a two-dimensional cellular automaton*, Physica A: Stat. Mech. Appl., **295** (2001), 507–525.
[14] S. Čanić, *On the influence of viscosity on Riemann solutions*, J. Dyn. Diff. Eqns., **10** (1998), 109–149.
[15] M. Chen, G. Bärwolff and H. Schwandt, *A derived grid-based model for simulation of pedestrian flow*, J. Zhejiang Univ.: Science A, **10** (2009), 209–220.
[16] E. Cristiani, B. Piccoli and A. Tosin, *Multiscale modeling of granular flows with application to crowd dynamics*, Multiscale Model. Simul., **9** (2011), 155–182.
[17] R. R. Clements and R. L. Hughes, *Mathematical modelling of a mediaeval battle: The battle of Agincourt, 1415*, Math. Comput. Simul., **64** (2004), 259–269.
[18] W. Daamen, P. H. L. Bovy and S. P. Hoogendoorn, *Modelling pedestrians in transfer stations*, in "Pedestrian and Evacuation Dynamics" (eds. M. Schreckenberg and S. D. Sharma), Springer-Verlag, Berlin, Heidelberg, (2002), 59–73.
[19] J. Esser and M. Schreckenberg, *Microscopic simulation of urban traffic based on cellular automata*, Int. J. Mod. Phys. C, **8** (1997), 1025–1036.
[20] A. D. Fitt, *The numerical and analytical solution of ill-posed systems of conservation laws*, Appl. Math. Modelling, **13** (1989), 618–631.
[21] H. Frid and I.-S. Liu, *Oscillation waves in Riemann problems inside elliptic regions for conservation laws of mixed type*, Z. Angew. Math. Phys., **46** (1995), 913–931.
[22] A. Harten, *Multiresolution representation of data: A general framework*, SIAM J. Numer. Anal., **33** (1996), 1205–1256.
[23] D. Helbing, I. Farkas and T. Vicsek, *Simulating dynamical features of escape panic*, Nature, **407** (2000), 487–490.
[24] D. Helbing, L. Buzna, A. Johansson and T. Werner, *Self-organized pedestrian crowd dynamics: Experiments, simulations, and design solutions*, Transportation Science, **39** (2005), 1–24.
[25] D. Helbing, I. Farkas and T. Vicsek, *Traffic and related self-driven many-particle systems*, Reviews of Modern Physics, **73** (2001), 1067–1141.
[26] H. Holden, *On the Riemann problem for a prototype of a mixed type conservation law*, Comm. Pure Appl. Math., **40** (1987), 229–264.
[27] S. P. Hoogendoorn and W. Daamen, *Self-organization in pedestrian flow*, Traff. Granul. Flow, **3** (2005), 373–382.
[28] R. L. Hughes, *A continuum theory for the flow of pedestrians*, Transp. Res. B, **36** (2002), 507–535.
[29] J. Hurley and B. J. Plohr, *Some effects of viscous terms on Riemann Problem solutions*, Math. Contemp., **8** (1995), 203–224.
[30] Y. Jiang, P. Zhang, S. C. Wong and R. Liu, *A higher-order macroscopic model for pedestrian flows*, Physica A, **389** (2010), 4623–4635.
[31] B. S. Kerner and P. Konhäuser, *Structure and parameters of clusters in traffic flow*, Physical Review E, **50** (1994), 54–83.
[32] B. L. Keyfitz, *A geometric theory of conservation laws which change type*, ZAMM Z. Angew. Math. Mech., **75** (1995), 571–581.
[33] B. L. Keyfitz, "Mathematical Properties of Nonhyperbolic Models for Incompressible Two-Phase Flow," Proceedings of the International Conference on Multiphase Flow, New Orleans, May 27–June 1, 2001, (CD-ROM).
[34] A. Kurganov and E. Tadmor, *New high-resolution central schemes for nonlinear conservation laws and convection-diffusion equations*, J. Comput. Phys., **160** (2000), 241–282.
[35] M. J. Lighthill and G. B. Whitham, *On kinematic waves. II. A theory of traffic flow on long crowded roads*, Proc. Roy. Soc. London Ser. A, **229** (1955), 317–345.
[36] A. Majda and R. L. Pego, *Stable viscosity matrices for system of conservation laws*, J. Diff. Eqns., **56** (1985), 229–262.
[37] D. Marchesin and B. Plohr, *Wave structure in WAG recovery*, SPE, paper 56480.
[38] S. Müller, "Adaptive Multiscale Schemes for Conservation Laws," Lecture Notes in Computational Science and Engineering, **27**, Springer-Verlag, Berlin, 2003.

[39] A. Nakayama, K. Hasebe and Y. Sugiyama, *Instability of pedestrian flow in 2D optimal velocity model with attractive interaction*, Comput. Phys. Comm., **177** (2007), 162–163.
[40] B. Piccoli and A. Tosin, *Time-evolving measures and macroscopic modeling of pedestrian flow*, Arch. Ration. Mech. Anal., **199** (2011), 707–738.
[41] P. I. Richards, *Shock waves on the highway*, Oper. Res., **4** (1956), 42–51.
[42] Th. Slawig, G. Bärwolff and H. Schwandt, "Hybrid macro-Microscopic Simulation of Pedestrian Flow," Technical report, Institut für Mathematik, Technische Universität Berlin, 2007.
[43] Th. Slawig, G. Bärwolff and H. Schwandt, "Simulation of Pedestrian Flows for Traffic Control Systems," in Proceedings of the 7th International Conference on Information and Management Sciences (IMS 2008) (Urumtschi, 12. 8. 08 - 19. 8. 08) (ed. E. Y. Li), California Polytechnic State University, Series on Information and Management Sciences, **7**, Pomona/California, 2008, 360–374.
[44] E. F. Toro, "Riemann Solvers and Numerical Methods for Fluid Dynamics. A Practical Introduction," Third edition, Springer-Verlag, Berlin 2009.
[45] Y. Xia, S. C. Wong, M. P. Zhang, C.-W. Shu and W. H. K. Lam, *An efficient discontinuous Galerkin method on triangular meshes for a pedestrian flow model*, Int. J. Numer. Meth. Engrg., **76** (2008), 337–350.
[46] P. Zhang, S. C. Wong and C.-W. Shu, *A weighted essentially non-oscillatory numerical scheme for a multi-class traffic flow model on an inhomogeneous highway*, J. Comput. Phys., **212** (2006), 739–756.

Received December 2010; revised June 2011.

E-mail address: sberres@uct.cl
E-mail address: ricardo.ruiz@epfl.ch
E-mail address: schwandt@math.tu-berlin.de
E-mail address: elmer@sherpasoftware.ca